Aperture-Dependent Injection of Ionospheric Perturbations Into Simulated SAR Data

Felipe Betancourt-Payan, Marc Rodriguez-Cassola, Pau Prats-Iraola, *Fellow, IEEE*, and Gerhard Krieger, *Fellow, IEEE*

***Abstract*— This letter presents an algorithm for the introduction of ionospheric disturbances into synthetic aperture radar (SAR) simulations in an aperture-dependent manner using subapertures. Its suitability is compared with other methods that follow the beam-center approximation. The method can be generalized to the injection of all kinds of disturbances, and its two main benefits are the accuracy of the squint angle accommodation inside the synthetic aperture and the possibility of neglecting the static ionosphere assumption. For example, realistic ionospheric disturbance maps (phase and intensity scintillation) are introduced into clutter images simulated for the Biomass mission. In this case, with a typical ionospheric irregularity height of 350 km, the limiting azimuth resolution of the irregularities to be injected is around 337 m.**

***Index Terms*— Ionosphere, ionospheric simulation, scintillation, synthetic aperture radar (SAR).**

I. Introduction

THE performance of low-frequency synthetic aperture radar (SAR) is affected by the dispersive nature of the ionosphere, which introduces time delay, phase advance, and Faraday rotation (FR) in the radar echoes, degrading the quality of the products [1], [2]. All these effects are related to the total electron content (TEC) experienced by the radar waves on their two-way propagation through the ionosphere [3], and the impact will also depend on the structure of the ionospheric irregularities. Turbulent plasma irregularities are responsible for fast phase and amplitude variations in radio signals (scintillation) and are mainly found at the F-layer of the ionosphere (with a peak altitude between 250 and 400 km) [4]. Observations have found ionospheric irregularities with outer scales starting at 5 km [5], [6], [7], [8]. Regarding the drift velocity, it has been reported, for example, that close to the Equator, the ionosphere drifts eastward at significant velocities at around 100–200 but also up to 400 m/s [9]. At the poles, the irregularities spiral around the magnetic field lines.

Simulations that account for the trans-ionospheric interaction must be conducted to study its impact on the SAR products and assess ionospheric mitigation algorithms. This can be done with the application of an Ionospheric Transfer Function (ITF) as described in [10] using a *beam-center* approximation: assuming that during the azimuth integration, the phase history of each pixel is only affected by the disturbance at the piercing point located at zero Doppler. Note that the ITF method is meant only to introduce disturbance in the phase history and intensity modulation of the raw data while the injection of the FR is missing. Different approaches to apply the ITF were found [11], [12]. However, the studies focused on the statistics of amplitude modulations rather than the accuracy of the injection of phase disturbances or the inclusion of FR.

It is also possible to introduce the effects on SAR data, which are *semi-focused* at ionospheric height [13] by adjusting the distances of closest approach and effective velocities in the azimuth matched filter. This operation accounts for the spatial variations in the ionospheric irregularities. However, it is still beam-centered as it acts as an averaging window equal to the size of the synthetic aperture (neglecting small structure perturbations) instead of allocating the disturbance as seen at each azimuth frequency for each position. The semi-focused approach also neglects propagation in the oblique directions, which introduces notable errors in wide-beam systems. In addition, both the beam-centered methods assume that the ionospheric scenario does not change (frozen ionosphere) or drift during the time of acquisition, and a fixed ionospheric height also constrains them.

Inspired by the knowledge of aperture-dependent motion compensation [14], [15], we present in this letter a new algorithm for the injection of ionospheric effects into simulated SAR images. It works with subapertures along the azimuth direction, allowing it to accommodate the distortion corresponding to the ionosphere portion that falls into the antenna beam for every satellite position. This way, one accounts for the angle variability and oblique propagation through the ionosphere and can also drop the frozen ionosphere and fixed ionospheric height assumptions. The performance of this method will be contrasted with the one of the semi-focusing, and simulation examples for the Biomass mission [16] will be presented. Compared with the beam-center approaches, this new algorithm can better accommodate the impact of irregularities that are of the order or smaller than the synthetic aperture at the ionospheric height (that for the case of Biomass is of ∼19 km). Because of blockwise implementation, the algorithm can be efficiently implemented and parallelized.

In Section II, the aperture-dependent principle and implementation will be presented. Section III shows a series of

Manuscript received 28 March 2024; revised 21 May 2024; accepted 23 May 2024. Date of publication 11 June 2024; date of current version 18 June 2024. This work was supported in part by the IEEE Publication Technology Department and in part by the German Academic Exchange Service (DAAD) under Grant 57478193. *(Corresponding author: Felipe Betancourt-Payan.)*

The authors are with the Microwaves and Radar Institute, German Aerospace Center (DLR), 82234 Wessling, Germany (e-mail: felipe.betancourtpayan@dlr.de).

Digital Object Identifier 10.1109/LGRS.2024.3411064

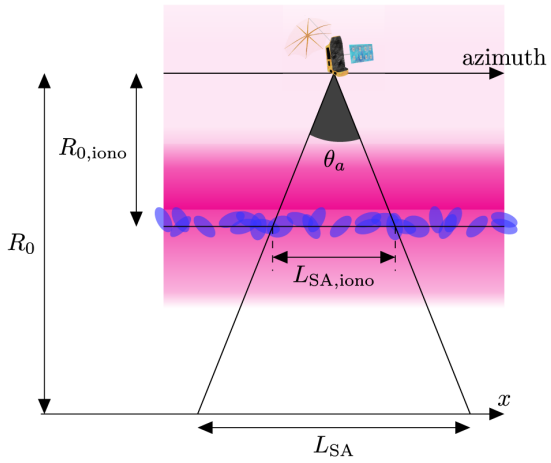

Fig. 1. Slant geometry of an SAR system through the ionosphere. The altitude-varying free electron density distribution is illustrated in pink, and the irregularities that can cause scintillation are shown in blue.

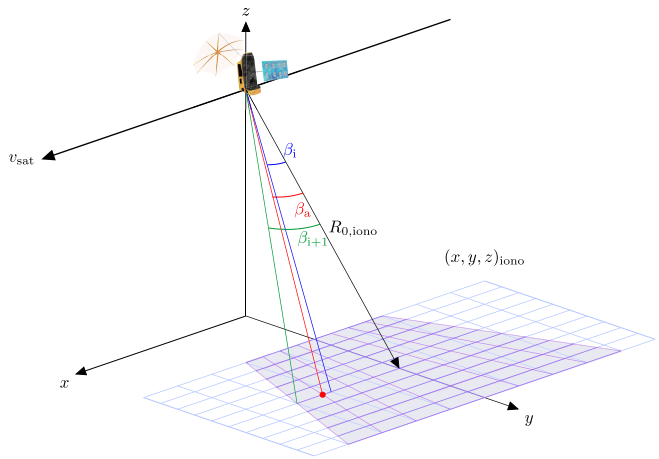

Fig. 2. Geometry at the ionospheric plane. The blue grid corresponds to the ionosphere, and the angular purple grid corresponds to the STFT of an azimuth subaperture. To obtain the unknown disturbance at the red piercing point in the direction of β_a (not known), a linear angle interpolation between β_i and β_{i+1} is necessary.

experimental results, and Section IV summarizes the results and draws conclusions.

II. Injection of Ionospheric Perturbations by Subapertures

In this section, we present an algorithm to incorporate high-frequency ionospheric perturbations into the simulation of SAR data. Fig. 1 shows the slant observation geometry of an SAR system through the ionosphere. For illustration purposes, a vertical free electron density distribution has been color-coded with shades of pink (darker means higher density at the altitude of the F-layer), and electron density irregularities are depicted around the area of maximum ionization. The slant range to the targets on the ground is R_0, θ_a is the azimuth angular aperture of the beam, and L_{SA} is the length of the synthetic aperture on the ground. For engineering and scientific applications of the scintillation theory, it has been proven that a phase screen model located at the height of maximum ionization, h_{iono}, well approximates more elaborated computations that include scattering across the vertical region [17], [18]. We will assume that the irregularities that cause scintillation are concentrated on a surface whose height might vary continuously, $h_{\text{iono}}(x)$, so that the variations are in general not negligible in high-resolution wide-beam systems and long acquisitions; therefore, the slant distance to the surface $R_{0,\text{iono}}$ and the approximate length of the synthetic aperture on the ionospheric surface $L_{\text{SA,iono}}$ can vary for each satellite position. A more complex scenario can be simulated with propagation through multiple phase screens [19], but that does not invalidate the method proposed in this letter.

Subapertures for Disturbance Injection: Based on available knowledge on aperture-dependent motion compensation [14], we propose an algorithm that uses subapertures for disturbance injection (SADI) to introduce ionospheric perturbations into SAR simulated images precisely. The principle is based on applying short-time Fourier transforms (STFTs) on partially overlapping blocks in the range-compressed data to exploit the relationship between azimuth frequency and squint angle

$$\sin(\beta_{\text{a}}[n]) = \frac{\lambda \cdot f_{\text{a}}[n]}{2 \cdot v_{\text{sat}}} \tag{1}$$

in small azimuth subapertures. This way, it is possible to accurately introduce the perturbations of the corresponding ionosphere portion that the beam sees for each satellite position (at the center of each subaperture). In (1), β_{a} is the azimuth squint angle from the beam center, λ is the wavelength, f_{a} is the azimuth frequency, and v_{sat} is the satellite velocity. n is the azimuth index in the STFT of each subaperture block.

Fig. 2 sketches the geometry of the ionospheric plane for one satellite position as seen at the center of a subaperture after an STFT (purple), together with the regular grid of the simulated ionosphere with coordinates $(x, y, z)_{\text{iono}}$ in blue. Without loss of generality, both the ionospheric perturbation and the radar beam can be sampled for a surface of changing altitude, and the satellite moves in an elliptical orbit. The angular purple grid illustrates the angular view of the beam with the polar coordinates $R_{0,\text{iono}}$ and β_{a}. The red dot along the red line denotes a piercing point, where the disturbance is not necessarily known but can be approximated by interpolation from the values at the known positions at the piercing points that correspond to β_i and β_{i+1}. A low-order angle interpolation is adequate to generalize the problem for nonflat surfaces with varying heights and downsample the ionosphere grid to the STFT resolution. The result will be referred as $\hat{\phi}(R_{0,\text{iono}}(h_{\text{iono}}), \beta_{\text{a}}; \lambda)$ for the phase and $\hat{\Omega}(R_{0,\text{iono}}(h_{\text{iono}}), \beta_{\text{a}}; \lambda)$ for the FR. Note that we highlight the dependency on λ to indicate that the method can be generalized to a nonmonochromatic wavefront, and on h_{iono} to indicate the variation in the layer inside the beam and along the acquisition. This way, it is possible to add for each frequency $f_{\text{a}}[n]$ (or each look angle $\beta_{\text{a}}[n]$ according to (1)) the disturbance that corresponds to the piercing point.

Fig. 3 shows a block diagram of the algorithm: For each satellite position, $p_{\text{sat}}[i]$, with the ionospheric surface

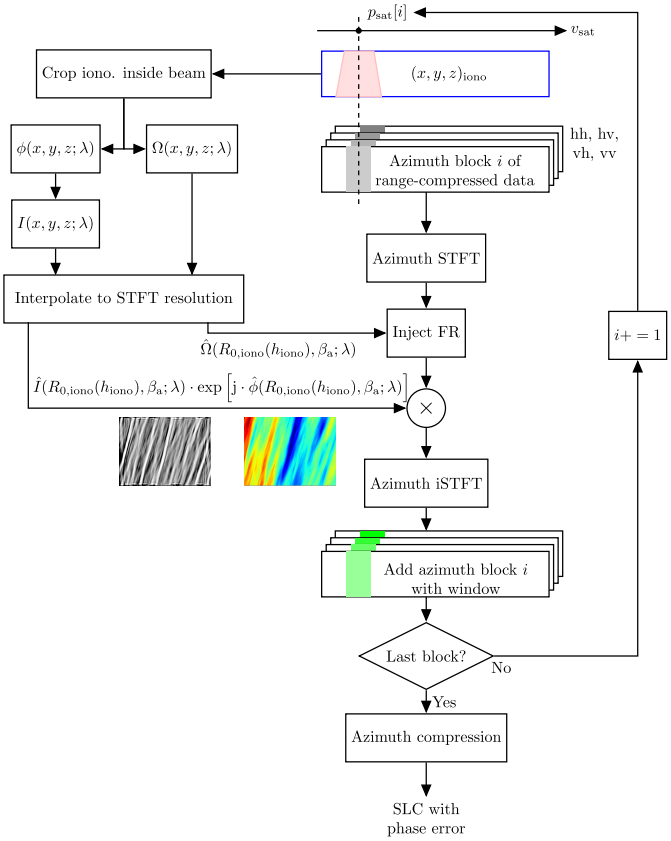

Fig. 3. Block diagram of the proposed aperture-dependent ionospheric injection algorithm.

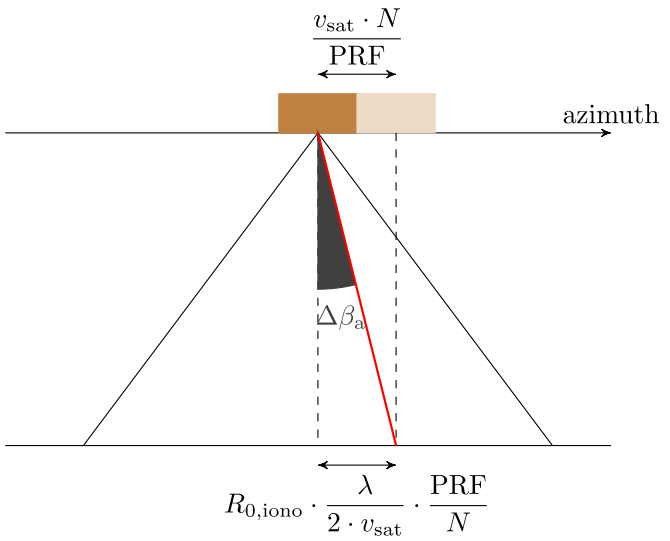

Fig. 4. Ionospheric irregularity resolution with azimuth subaperture size. Flight track (top) with the platform displacement across a subaperture and ionospheric irregularity plane (bottom). The differential squint angle $\Delta\beta_{\text{a}}$, which is given by the subaperture size N, determines the spatial resolution of the ionospheric plane.

coordinates, the part of the ionosphere that falls inside the beam is calculated. Before the downsampling step, from the local phase disturbance seen by the beam, it is possible to simulate the corresponding double-pass amplitude modulation approximating it to the absolute value of the split-step solution of a monochromatic wave that goes through a phase disturbance as described in [12]. Similar to [10], it is assumed that the ionosphere modulation can be pulled out of the summation over all the targets that make the range-compressed data, but given the subaperture operation proposed in this letter, without the small target assumption.

On the left side of Fig. 3, an example of the phase and intensity scintillation component corresponding to one subaperture is shown. Now, the local FR, phase, and intensity *screens* are downsampled and interpolated to the STFT resolution before injection. Around the corresponding satellite azimuth position index in the range-compressed image, an STFT is done (in this case, for the data from all the polarimetric channels). First, the local FR disturbance and then the phase and intensity are injected before using an inverse STFT to bring the subaperture back to the time domain. The range-compressed solution with ionospheric disturbances is built up by adding all subapertures, each with a window to maintain the power of the data. The steps are repeated in a loop to the last azimuth position. After building a range-compressed image, the data are compressed with a matched filter in azimuth to obtain single-look complex (SLC) images with the ionospheric disturbances.

The last thing to discuss is the number of pulses N in the subaperture, which is related to the azimuth frequency resolution, (PRF/N), and ultimately to the differential squint angle $\Delta\beta_{\text{a}}$ in Fig. 4 (note that we are making use of $\sin\beta_{\text{a}} \approx \beta_{\text{a}}$ approximation for small angles in (1)). To ensure consistency, the spatial sampling $(v_{\text{sat}} \cdot N)/\text{PRF}$, locally increased by the block operation, shall be matched to the reduced spatial frequency resolution at which the ionospheric coordinates are sampled, which is also driven by the distance to the ionospheric plane, $R_{0,\text{iono}} \cdot (\lambda \cdot \text{PRF})/(2 \cdot v_{\text{sat}} \cdot N)$, i.e.,

$$N = \sqrt{\frac{R_{0,\text{iono}} \cdot \lambda}{2}} \cdot \frac{\text{PRF}}{v_{\text{sat}}}. \tag{2}$$

The corresponding resolution, the scale of the smallest irregularities that can be detected, is given by the following equation:

$$\delta_x = \sqrt{\frac{R_{0,\text{iono}} \cdot \lambda}{2}}. \tag{3}$$

The Biomass mission parameters described in Table I give an azimuth block size N of approximately 70 pixels. These correspond to an azimuth resolution of 337.92 m at an ionospheric height of 350 km.

III. Experimental Results

In this section, the performance of the beam-center approach described in [13] for the injection of ionospheric disturbances will be compared with the aperture-dependent one proposed in this letter. For the simulations, a complex clutter scenario is used. With the thin-layer approximation, phase advance maps that follow a power spectral density (PSD) function can be generated as described in [10] and [20]. Two representative maps at two different geographic locations are shown in Fig. 5 generated with the parameters in Table II. $C_k L$ and p are

TABLE I

SYSTEMS PARAMETERS

Parameter	Units	Biomass
Carrier frequency f_0	Hz	$435 \cdot 10^6$
Carrier wavelength λ	m	0.69
Satellite height h_{sat}	km	650
Ionospheric height h_{iono}	km	350
Satellite velocity v_{sat}	km/s	7.534
Antenna azimuth length L_{a}	m	12
Incidence angle θ_{inc}	deg	25
Range to ionosphere $R_{0,\mathrm{iono}}$	km	331
Pulse repetition frequency PRF	Hz	1581.03
Azimuth bandwidth B_{a}	Hz	1255.79
Synthetic aperture L_{SA}	km	41.19
Synthetic aperture at ionosphere $L_{\mathrm{SA,iono}}$	km	19.01

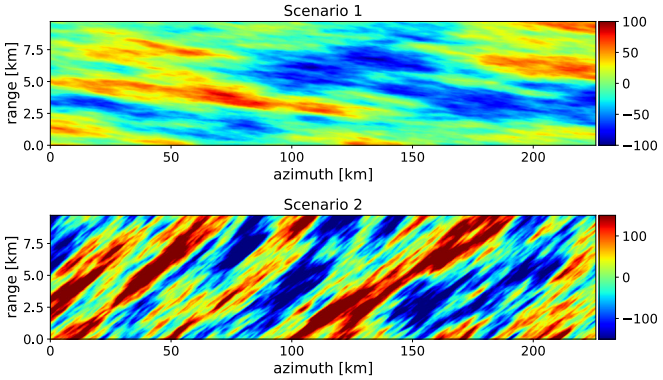

Fig. 5. Phase maps used in the simulations. Generated with Rino's method and the parameters in Table II.

TABLE II

PHASE MAP PARAMETERS

Parameter	Units	Scenario 1	Scenario 2
Geographic location (lat, lon)	(deg, deg)	14.5, 10.5	-25.5, -22
Outer scale L_0	km	10	8
Strength of turbulence $C_k L$	-	10^{32}	10^{33}
Anisotropy parameter a	-	10	10
Anisotropy parameter b	-	1	1
Spectral index p	-	2.65	2.65

related to the strength and granularity of the irregularities, a and b to the anisotropy, and the outer scale L_0 is the scale size of the bigger irregularities. Note that despite the size of the outer scale, there would be plenty of smaller scale irregularities up to the order of a few meters. The scenarios and the exact geometry have been defined using the Biomass End-to-End Performance Simulator (BEEPS) [21].

The first step in comparing the beam-centered approach and SADI is to show that both the methods give similar results when the irregularities are much larger in the azimuth dimension than the synthetic aperture projected on the ionosphere. For that, we use the phase map in Scenario 1 (Fig. 5), where irregularities change slowly due to the high anisotropy compared with the synthetic aperture. Fig. 6 shows two interferograms that compare the unperturbed image for the beam-center approach (top) and the SADI approach. Note that in both the cases, the output is a smoothed version of Scenario 1 due to the synthetic aperture convolution, and the interferograms look identical, so the improvement in resolution is not perceived. This is better appreciated in Fig. 7 where the phase difference is shown (nearly 0 everywhere).

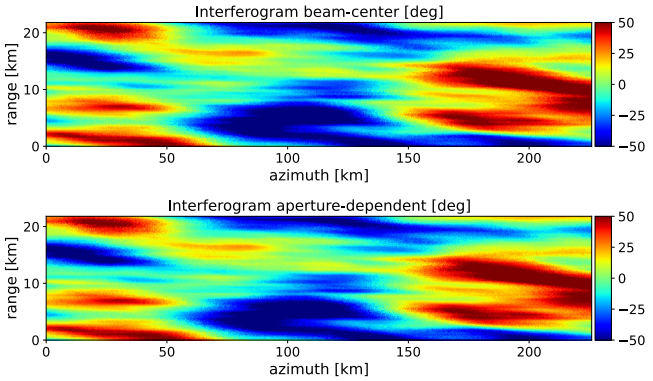

Fig. 6. Interferograms between images before and after the injection of the phase map in Scenario 1 with the beam-center method (top) and SADI (bottom).

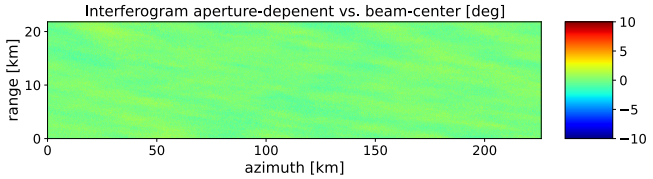

Fig. 7. Phase difference between the output of both the methods in Scenario 1.

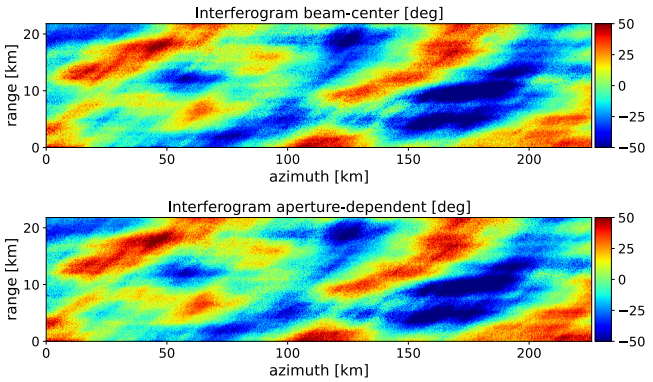

Fig. 8. Interferograms between images before and after the injection of the phase map in Scenario 2 with the beam-center method (top) and SADI (bottom).

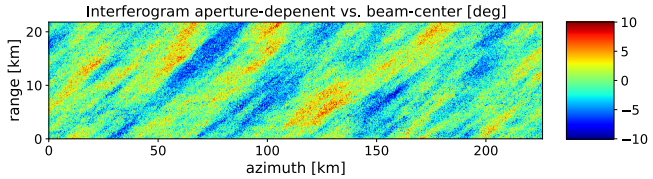

Fig. 9. Phase difference between the output of both the methods in Scenario 2.

We compare the results when the phase map in Scenario 2 (Fig. 5) is used. Here, despite the large anisotropy, due to the geomagnetic field orientation, the size of the irregularities in the azimuth direction is small compared with the synthetic aperture. The resolution increment is not visible in Fig. 8 but in Fig. 9, which shows the phase difference between both the interferograms. Here, one can see that the difference between both the methods is the high-frequency component of the phase, which was averaged by the beam-center approximation but not by the SADI technique.

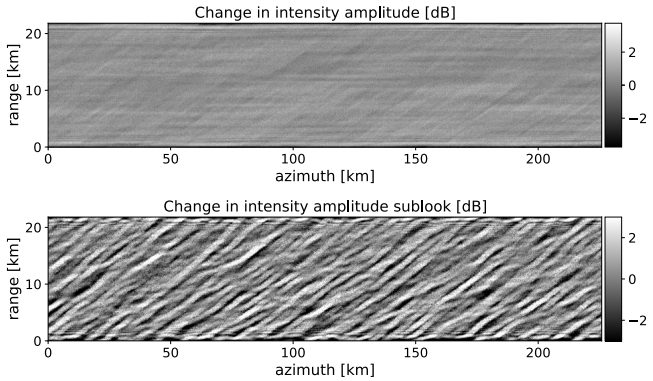

Fig. 10. Intensity scintillation in focused image with ionospheric disturbance (top), 1/10 bandwidth sublook (bottom).

The results in Fig. 10 show the intensity scintillation corresponding to Scenario 2, the focused image, and the intensity of one sublook. Note the appearance of the stripes in the sublooked image and that the orientation is maintained with respect to the phase screen with a higher frequency variation as expected.

IV. Conclusion

This letter has presented a method for incorporating ionospheric disturbances into SAR simulations in an aperture-dependent manner. This approach is preferred over other beam-center methods like applying an ITF or semi-focusing at ionospheric height previously discussed in the literature because it allows to accommodate ionospheric realizations with a varying height or which are quickly changing with time. It works with subapertures and introduces the ionospheric disturbance for each satellite position that, at the instant, falls inside the antenna beam while it adapts the geometry. It also takes into account the oblique propagation out of the beam center. This makes it possible to gain resolution when ionospheric irregularities smaller than the synthetic aperture projected on the ionosphere are present, making it fit for wide-beam systems. This was shown in realistic simulation scenarios in the framework of the Biomass mission. Injection of intensity scintillations was also proved possible. This approach can be generalized to inject all kinds of disturbances. Here, we commented on the possibility of injecting FR, but it would be possible to inject dispersion and time delays, too.

References

[1] N. C. Rogers, S. Quegan, J. S. Kim, and K. P. Papathanassiou, "Impacts of ionospheric scintillation on the BIOMASS P-band satellite SAR," *IEEE Trans. Geosci. Remote Sens.*, vol. 52, no. 3, pp. 1856–1868, Mar. 2014.

[2] F. J. Meyer and J. Nicoll, "The impact of the ionosphere on interferometric SAR processing," in *Proc. IEEE Int. Geosci. Remote Sens. Symp. (IGARSS)*, vol. 2, Jul. 2008, p. 391.

[3] Z.-W. Xu, J. Wu, and Z.-S. Wu, "A survey of ionospheric effects on space-based radar," *Waves Random Media*, vol. 14, no. 2, pp. S189–S273, Apr. 2004.

[4] J. Aarons, "Global morphology of ionospheric scintillations," *Proc. IEEE*, vol. 70, no. 4, pp. 360–378, Apr. 1982.

[5] Y.-H. Liu, C.-H. Liu, and S.-Y. Su, "Global and seasonal scintillation morphology in the equatorial region derived from ROCSAT-1 in-situ data," *Terr., Atmos. Ocean. Sci.*, vol. 23, no. 1, p. 95, 2012.

[6] S. Basu, S. Basu, and B. K. Khan, "Model of equatorial scintillations from in-situ measurements," *Radio Sci.*, vol. 11, no. 10, pp. 821–832, Oct. 1976.

[7] K. C. Yeh and C. H. Liu, "Diagnosis of the turbulent state of ionospheric plasma by propagation methods," *Radio Sci.*, vol. 12, no. 6, pp. 1031–1034, Nov. 1977.

[8] C. L. Rino and J. Owen, "Numerical simulations of intensity scintillation using the power law phase screen model," *Radio Sci.*, vol. 19, no. 3, pp. 891–908, May 1984.

[9] S. Ji, W. Chen, X. Ding, and C. Zhao, "Equatorial ionospheric zonal drift by monitoring local GPS reference networks," *J. Geophys. Res.*, vol. 116, 2011, Art. no. A08310, doi: 10.1029/2010JA015993.

[10] C. S. Carrano, K. M. Groves, and R. G. Caton, "Simulating the impacts of ionospheric scintillation on L band SAR image formation," *Radio Sci.*, vol. 47, no. 4, pp. 1–14, Aug. 2012.

[11] N. Rogers and P. Cannon, "The synthetic aperture radar trans-ionospheric radio propagation simulator (SAR-TIRPS)," in *Proc. IRST*, Apr. 2009, pp. 1–5.

[12] F. J. Meyer, K. Chotoo, S. D. Chotoo, B. D. Huxtable, and C. S. Carrano, "The influence of equatorial scintillation on L-band SAR image quality and phase," *IEEE Trans. Geosci. Remote Sens.*, vol. 54, no. 2, pp. 869–880, Feb. 2016.

[13] J. S. Kim, K. P. Papathanassiou, R. Scheiber, and S. Quegan, "Correcting distortion of polarimetric SAR data induced by ionospheric scintillation," *IEEE Trans. Geosci. Remote Sens.*, vol. 53, no. 12, pp. 6319–6335, Dec. 2015.

[14] P. Prats, A. Reigber, and J. J. Mallorqui, "Topography-dependent motion compensation for repeat-pass interferometric SAR systems," *IEEE Geosci. Remote Sens. Lett.*, vol. 2, no. 2, pp. 206–210, Apr. 2005.

[15] M. Rodriguez-Cassola et al., "Doppler-related distortions in Tops SAR images," *IEEE Trans. Geosci. Remote Sens.*, vol. 53, no. 1, pp. 25–35, Jan. 2015.

[16] *Report for Mission Selection: Biomass*, document ESA SP-13214/1, European Space Agency (ESA), Noordwijk, The Netherlands, Nov. 2012.

[17] C. L. Rino, "On the application of phase screen models to the interpretation of ionospheric scintillation data," *Radio Sci.*, vol. 17, no. 4, pp. 855–867, Jul. 1982.

[18] E. N. Bramley, "The accuracy of computing ionospheric radio-wave scintillation by the thin-phase-screen approximation," *J. Atmos. Terr. Phys.*, vol. 39, no. 3, pp. 367–373, Mar. 1977.

[19] D. L. Knepp, "Multiple phase screen calculation of two-way spherical wave propagation in the ionosphere," *Radio Sci.*, vol. 51, no. 4, pp. 259–270, Apr. 2016.

[20] C. L. Rino, "A power law phase screen model for ionospheric scintillation: 1. Weak scatter," *Radio Sci.*, vol. 14, no. 6, pp. 1135–1145, Nov. 1979.

[21] M. J. Sanjuan-Ferrer et al., "End-to-end performance simulator for the BIOMASS mission," in *Proc. 12th Eur. Conf. Synth. Aperture Radar (EUSAR)*, Jun. 2018, pp. 1–5.